The Energy Budget of the Polar Atmosphere in MERRA

RICHARD I. CULLATHER
Earth System Science Interdisciplinary Center, University of Maryland, College Park

MICHAEL G. BOSILOVICH
Global Modeling and Assimilation Office,
NASA Goddard Space Flight Center, Greenbelt, Maryland

Submitted to: *Journal of Climate*

→ Do not distribute ←

Corresponding author address: Richard Cullather, % NASA/GSFC Code 610.1,
8800 Greenbelt Road, Greenbelt, MD 20771.
E-mail: richard.cullather@nasa.gov

ABSTRACT

A quantitative estimate of the atmospheric energy budget is useful for understanding rapidly changing conditions in the high latitudes. Here, components of the atmospheric energy budget from the Modern Era Retrospective-analysis for Research and Applications (MERRA) are evaluated in polar regions for the period 1979-2005 and compared with previous estimates and in situ observations. For the annual mean, the north polar cap bounded by 70°N is characterized in MERRA by a horizontal flux convergence of 99±4 W m^{-2}, a surface net flux of 19±1 W m^{-2} and a loss of 110±1 W m^{-2} from the top of the atmosphere (TOA). The south polar cap is characterized by a convergence of 118±6 W m^{-2}, a surface net flux of 3±1 W m^{-2} and a TOA loss of 101±1 W m^{-2}. Substantial differences are found between MERRA and previous estimates of the net surface energy flux. In the Arctic, comparison with observations from the Surface Heat Budget of the Arctic ice camp field study indicates spring time radiative flux differences that are associated with an overly simplistic representation of sea ice albedo, while a downwelling longwave flux bias of 12 W m^{-2} is found throughout the year. In the Antarctic, deficiencies in the representation of the subsurface energy flux result in an annual mean imbalance over grounded ice. Comparisons with values observed at South Pole indicate large discrepancies in downwelling radiative flux components. Despite these differences, MERRA compares favorably to previous studies of the annual cycle of atmospheric energy transport, convergence, and the total atmospheric energy tendency in the polar regions.

1. Introduction

The objective of this study is to examine the performance of the Modern Era Retrospective-analysis for Research and Applications (MERRA) in representing the high latitude atmospheric energy budget. MERRA was recently released by NASA's Global Modeling and Assimilation Office (GMAO). This effort, as well as a companion paper examining the atmospheric moisture budget (Cullather and Bosilovich, 2010), represent an initial examination of this reanalysis in the polar regions.

A quantitative knowledge of the flow, storage, and conversion of energy within the climate system has evolved with time as a result of contributions made by improvements in the observing system and by numerical atmospheric reanalyses (e.g., Fasullo and Trenberth, 2008). In the polar regions the energy budget and its variability is frequently used as a diagnostic for understanding rapidly changing conditions including glacial mass balance and perennial sea ice reduction (e.g., Porter et al., 2010). As noted in Cullather and Bosilovich (2010), numerical reanalyses are widely used in polar research for evaluating polar processes, as boundary conditions for limited area atmosphere and ice/ocean models, and as a first-order validation for climate models. However reanalyses inevitably contain inaccuracies resulting from the limitations in the observing system, inconsistencies between differing observations, and incomplete knowledge of the physical processes that are represented in the assimilating weather forecast model. In particular, surface albedo characteristics over polar oceans and high latitude cloud properties are both associated with important but complex energy feedback mechanisms that have historically been poorly simulated (Randall et al., 1998). An initial evaluation of the high latitude energy budget in a reanalysis record is therefore a constructive activity.

Some questions of interest pertaining to this study are as follows.

- What are the spatial and temporal patterns of energy budget components in MERRA, and how do they compare with previous studies?
- How do MERRA surface fluxes compare with in situ field studies?
- What is the nature of adjustment terms in the energy budget?

Section 2 provides an overview of the MERRA data set and method. An evaluation of the atmospheric energy balance in polar regions is given in section 3. A discussion of these comparisons is then given in section 4.

2. Numerical sets and method

A description of the MERRA system is given by Cullather and Bosilovich (2010) and Rienecker et al. (2010), and is summarized here. The MERRA collection was made using the Data Assimilation System component of the Goddard Earth Observing System (GEOS DAS, Rienecker et al., 2009), and covers the modern satellite era from 1979 to the present. The assimilation system utilizes the GEOS model, version 5 (GEOS-5)– a finite-volume atmospheric general circulation model (AGCM) that is used for operational numerical weather prediction. For MERRA, the GEOS DAS was run at a horizontal resolution of 2/3° longitude by 1/2° latitude and 72 hybrid-sigma coordinate vertical levels to produce an observational analysis at 6-hour intervals. Boundary conditions include climatological aerosol and solar forcing. Sea surface temperature and sea ice are linearly interpolated in time from weekly 1-degree resolution Reynolds fields (Reynolds, 2002). A 50 percent sea ice fraction threshold is used to distinguish ice from open water for the radiative transfer model. The atmospheric model is coupled to a catchment-based hydrologic model on land (Koster et al., 2000) and a sophisticated multi-layer snow model (Stieglitz et al., 2001) that is coupled to the catchment hydrology. Land-surface albedos are derived from MODIS retrievals (Moody et al., 2005).

MERRA utilizes the incremental analysis update assimilation method (IAU; Bloom et al., 1996), which is described in Cullather and Bosilovich (2010). The IAU variable is a tendency that quantifies the difference between an initial 6-hourly analysis field and the background forecast model state. The forecast model is then run over the six-hour interval using this tendency as an additional forcing term. The resulting MERRA product is then composed of dynamically-consistent one-hourly fields that are incrementally corrected to observation every six hours. The sum of IAU variables quantify the adjustment terms in atmospheric balance equations. Thus atmospheric budgets– as they are constructed in the GEOS-5 AGCM– and their incremental adjustments are maintained within MERRA to the accuracy limited by round-off and data compression errors.

From Cullather and Bosilovich (2010), the atmospheric moisture budget for MERRA may be written as

$$\begin{aligned}\frac{\partial (W_v + W_l + W_i)}{\partial t} + \nabla \cdot \left\{ \int_{P_{top}}^{P_{sfc}} \frac{(q_v + q_l + q_i)}{g} \cdot \tilde{\mathbf{V}}\, dp \right\} \\ = E - P + \left.\frac{\partial W_v}{\partial t}\right|_{CHM} + \left.\frac{\partial (W_v + W_l + W_i)}{\partial t}\right|_{FIL} + \varepsilon_{IAU(M)}\end{aligned} \qquad (1)$$

where

$$W_{(v,l,i)} = \frac{1}{g} \int_{P_{top}}^{P_{sfc}} q_{(v,l,i)}\, dp\ . \qquad (2)$$

Here, W_v is precipitable water, W_l is total cloud liquid condensate in the atmospheric column, W_i is total cloud ice condensate in the atmospheric column, q_v is specific humidity, q_l is cloud liquid water mixing ratio, q_i is cloud ice mixing ratio, P_{sfc} is surface pressure, P_{top} is the fixed pressure of the top model level which is 0.01 hPa, $\tilde{\mathbf{V}}$ is the horizontal wind vector, and g is the gravity constant. The symbol E represents the net of evaporation minus deposition of hoar frost, P is total (solid plus convective and large-scale liquid) precipitation, and $\varepsilon_{IAU(M)}$ is the quantity imposed by the incremental analysis update on the moisture budget. The first term on the left-hand-side represents a temporal derivative and is given by the summation of three MERRA variables for each water species denoting contributions from model dynamics, physical parameterizations, and the IAU. On the right-hand side, the term denoted by "*CHM*" represents a parameterized source of water vapor in the middle atmosphere from the model chemistry routine and is small (Suarez et al., 2010). The notation "*FIL*" refers to tendencies associated with the "filling" of spurious negative water, which was found to be negligible.

Following a form similar to Trenberth (1997), the total energy equation integrated over the atmospheric column for MERRA may be written as

$$\frac{\partial A_E}{\partial t} + \nabla \cdot \tilde{\mathbf{F}}_A = R_{top} + F_{sfc} + L_v \left.\frac{\partial W_v}{\partial t}\right|_{CHM} + \left[L_v \frac{\partial W_v}{\partial t} - L_f \frac{\partial W_i}{\partial t} \right]_{FIL} + \varepsilon_{IAU(E)} - Q_{NUM} \,. \qquad (3)$$

Note the contribution of latent heating terms from equation (1) in (3). For the MERRA energy budget, the time rate of change in total atmospheric energy storage A_E is expressed as

$$\frac{\partial A_E}{\partial t} = L_v \frac{\partial W_v}{\partial t} - L_f \frac{\partial W_i}{\partial t} + \frac{\partial}{\partial t} \left\{ \frac{1}{g} \int_{P_{top}}^{P_{sfc}} (c_P T_v + \Phi_S + k)\, dp \right\} \quad , \qquad (4)$$

where the assumed constant L_v is the latent heat of vaporization, L_f is the latent heat of fusion, c_P is the specific heat of the atmosphere at constant pressure, T_v is virtual temperature, Φ_S is surface geopotential, and $k = \frac{1}{2}\left|\tilde{\mathbf{V}}\right|^2$ is kinetic energy. The product $c_p\, T_v$ is referred to as virtual enthalpy. The divergence term may be expanded as follows:

$$\nabla \cdot \tilde{\mathbf{F}}_A = \nabla \cdot \frac{1}{g}\int_{P_{top}}^{P_{sfc}} (L_v q_v - L_f q_i)\tilde{\mathbf{V}}\, dp + \nabla \cdot \frac{1}{g}\int_{P_{top}}^{P_{sfc}} c_P T_v \cdot \tilde{\mathbf{V}}\, dp + \nabla \cdot \frac{1}{g}\int_{P_{top}}^{P_{sfc}} \Phi \cdot \tilde{\mathbf{V}}\, dp + \nabla \cdot \frac{1}{g}\int_{P_{top}}^{P_{sfc}} k \cdot \tilde{\mathbf{V}}\, dp \quad , \quad (5)$$

where Φ is geopotential within the atmospheric column. The second integral on the right hand side of (5) is referred to as the divergence of dry static energy; the first three integrals on the right hand side are referred to as the divergence of moist static energy. The boundary conditions of (3) are given as

$$R_{top} = SW_{top} + LW_{top} \quad , \qquad (6)$$

where SW_{top} and LW_{top} are the net downward shortwave and longwave radiative fluxes at the top of the atmosphere (TOA), and

$$F_{sfc} = Q_H + Q_E + L_f P_s - R_{sfc} \quad , \qquad (7)$$

where Q_H and Q_E are the upwards surface turbulent sensible and latent heat fluxes, the product $L_f P_s$ is latent heating resulting from solid precipitation, and R_{sfc} is the net downward radiative flux at the surface. The term for latent heat from solid precipitation is typically not included in other studies. Again, $\varepsilon_{IAU(E)}$ is the tendency imposed by the incremental analysis update, in this case for the energy budget, and represents the summation of latent heat, virtual enthalpy, kinetic, and geopotential energy term contributions. Finally, Q_{NUM} in equation (3) denotes the contribution of spurious residuals resulting from inertial terms, the discretization of the thermodynamic equation, coordinate remapping during model integration, and time-truncation errors. The global mean of these terms are used by the dynamical core of the assimilating model, however the horizontal distribution is locally significant– particularly over steep topography– and must be accounted for. The quantity Q_{NUM} is then computed from MERRA variables as the net difference between local contributions and the global mean. The relation between MERRA variables and equation notation is detailed in the appendix.

The approach of this study is to evaluate MERRA values against prior studies for large-scale areal averages of the terms in (3-7) over fixed polar regions as shown in Fig. 1, with a particular focus on the polar caps. Historically, budgets of the polar caps have been defined using the 70° parallels as boundaries that roughly correspond to geographical contrasts between land and ocean and a local maximum in the coverage of the in situ observing network. An Arctic Ocean domain is also utilized to roughly correspond with a recent study (Serreze et al., 2007). Finally, a Southern Ocean fixed domain is determined by the farthest north wintertime sea ice edge.

Studies for comparison include Nakamura and Oort (1988), Genthon and Krinner (1998), Serreze et al. (2007), and Porter et al. (2010). Nakamura and Oort (1988) produced budget estimates for both polar caps using the ocean flux values of Levitus (1984), composite satellite data from the period 1966-1977, and atmospheric circulation statistics from Oort (1983) which are largely based on the upper air station network. Nakamura and Oort (1988) found the observational network insufficient for computing atmospheric energy transport into the south polar cap and instead produced output from the NOAA Geophysical Fluid Dynamics Laboratory GCM. Genthon and Krinner (1998) used the 15 year re-analysis of the European Centre for Medium-Range Weather Forecasts (ECMWF) (ERA-15; Gibson et al., 1997) for the period 1979-1993 to evaluate the south polar cap. Serreze et al. (2007) examined the north polar cap and Arctic Ocean domains using the more recent 40 year re-analyis of ECMWF (ERA-40; Uppala et al., 2005) and the National Centers for Environmental Prediction/National Center for Atmospheric Research Reanalyses (NCEP/NCAR; Kalnay et al., 1996) for the period 1979-2001. Serreze et al. (2007) also examined TOA radiative fluxes from the Earth Radiation Budget Experiment for the study period February 1985 to April 1989 (ERBE; Barkstrom, 1984). Porter et al. (2010) similarly examined the north polar cap energy budget for the period November 2000 to October 2005 using the 25-year Japanese Re-Analysis (JRA-25; Onogi et al., 2007), and satellite data from the Clouds and the Earth's Radiant Energy System (CERES; Wielicki et al., 1996) product. In support of these budget comparisons, the evaluation of near-surface state variables against station observations is also instructive.

Evidence of an evolving climate system in polar regions– particularly for the Arctic (e.g., Porter et al., 2010)– motivate an exclusion of the most recent years in the time series. The results presented here are for the period 1979-2005, however MERRA values concurrent with previous studies are applied when useful. When appropriate, the standard deviation of mean estimates is presented as the uncertainty value (i.e., the mean ± the standard deviation).

3. Atmospheric energy budget

a. Balance adjustment quantities

Terms of the atmospheric energy budget averaged over the period 1979-2005 from MERRA are shown in Table 1 for the polar regions defined in Fig. 1. The far right column indicates budget adjustment quantities. As noted earlier, artificial moisture filling and chemistry parameterization terms of the energy budget from equation (3) have essentially zero magnitude. Not shown, the spatial pattern of the spurious residual Q_{NUM} is characterized by alternating positive and negative values in regions of steep topography. Averages taken over limited areas may produce aliasing of these oscillating values. For example, Q_{NUM} averages 1.5±0.2 W m^{-2} over the Greenland Ice Sheet. But in general, the incremental analysis update is the largest adjustment quantity of interest in the atmospheric energy budget, and its spatial patterns are shown in Fig. 2. Here, positive values indicate an energy surplus in the balance equation while negatives indicate a deficit. The magnitude is a measure of closure obtainable by physical terms. The spatial patterns shown in Fig. 2 are complex, vary with time, and are typically dissimilar to the patterns of the IAU for the atmospheric moisture budget shown by Cullather and Bosilovich (2010).

As noted previously, the total IAU for the energy budget is the summation of contributions from latent heat, virtual enthalpy, kinetic, and geopotential energy terms. Of these four, the contribution to the IAU term from virtual enthalpy is large for monthly and annual averages in both polar cap regions, while the IAU from latent heating is also significant for the north polar cap. For the Northern Hemisphere polar region, negative values for the IAU are found over the Arctic Ocean, while positive values are present over surrounding lower latitudes. Mean annual amounts less than –40 W m^{-2} are present in the vicinity of the North Pole with smaller magnitudes over Greenland and marginal seas. Seasonally, these magnitudes are larger in summer than in winter, however the values do not approach the local imbalances of greater than 100 W m^{-2} that are shown for the ERA-40 in Serreze et al. (2007). For the average over the north polar cap, the IAU ranges from –4 W m^{-2} in February to –17 W m^{-2} in June, as may be seen in Fig. 3(a).

In Cullather and Bosilovich (2010), the MERRA IAU for the atmospheric moisture budget was shown to be characterized by closed contours denoting upper air stations in coastal Greenland and Antarctica. Although signatures of upper air station locations are not as evident in the MERRA energy budget IAU as in the IAU field for the atmospheric moisture budget, a dipole is apparent in Fig. 2(a) in the vicinity of Hudson Strait with centers near Kuujjuaq (58°N, 68°W) and Cape Dorset (64°N, 77°W). Averaged over the north polar cap and the period 1979-2005, $\varepsilon_{IAU(E)}$ is –11 W m^{-2}. The temporal variability of the IAU for the energy budget in the

Arctic also differs markedly from the IAU of the atmospheric moisture budget. Changes in the atmospheric moisture budget IAU were largely found to be associated with changes to the observing system in November 1998 and October 2001. In particular, the November 1998 change is associated with the introduction of AMSU and has been noted in surface moisture fluxes in other reanalyses (Saha, 2010). In contrast, the MERRA energy budget IAU time series for the north polar cap indicates changes which are not concurrent with satellite observing system changes. The magnitude of the energy budget IAU averages less than 10 W m^{-2} for the period 1979-1991, approximately 18 W m^{-2} over the period 1992-1997, and 9 W m^{-2} thereafter. These shifts may be due to changes in the surface observing system or in the atmospheric circulation.

In the Southern Hemisphere, the MERRA IAU term for the energy budget as shown in Fig. 2(b) has a larger magnitude than for the north polar cap, with magnitudes of greater than 80 W m^{-2} over Victoria Land and regions of northern Queen Maud Land in East Antarctica. Over the south polar cap, the IAU ranges from –27 W m^{-2} in February to –20 W m^{-2} in August and September. The annual average IAU is comparatively smaller over the lower latitudes of the Southern Ocean as seen in Fig. 2(b). There is a considerable annual cycle for the Southern Ocean domain ranging from –40 W m^{-2} in January and February to –9 W m^{-2} in June. The field mostly indicates energy deficits, which are largest on the annual cycle during the equinoxes. The year to year time series for the south polar cap is highly variable and ranges from –37 W m^{-2} in 1983 to –9 W m^{-2} in 1998. The IAU time series for the south polar cap energy budget is uncorrelated with that of the north polar cap, and its relation to changes in the observing system is not as readily apparent. Over the data-sparse Southern Ocean domain there is a discontinuity in the IAU time series in 1998 that is likely associated with the introduction of AMSU. The Southern Ocean IAU averages –21.8 W m^{-2} prior to 1998, and –26.7 W m^{-2} thereafter.

b. Total atmospheric energy tendency

In both the north and south polar caps, the MERRA total energy tendency is near zero for annual averages and is small for months of solstice, as shown in Table 1. But there is an oscillatory annual cycle for the tendency terms as seen in Fig. 3. For the north polar cap, the tendency term reaches a maximum of 26±11 W m^{-2} in April and a minimum of –26±9 W m^{-2} in September. This annual cycle agrees very closely with values from other reanalyses as reported by Porter et al. (2010), Serreze et al. (2007), and from the observational study of Nakamura and Oort (1988). The RMS difference of monthly means with MERRA is only 4 W m^{-2} for both NCER/NCAR and the Japanese Re-Analysis (JRA-25; Onogi et al., 2007) as reported by Porter et al. (2010), less than 1 W m^{-2} for the ERA-40 as reported by Serreze et al. (2007), but 10 W m^{-2} for Nakamura and Oort (1988). In general the reanalyses are more similar to each other than to the Nakamura and Oort time series.

For the south polar cap, the total energy tendency in MERRA ranges from a minimum of -16±12 W m^{-2} in April to 30±16 W m^{-2} in November. As seen in Fig. 3(b), the annual cycle is less sinusoidal than in the Northern Hemisphere, with the November peak offsetting an average negative tendency that extends from January through July. The RMS difference with monthly values reported by Nakamura and Oort (1988) as compared to MERRA is 13 W m^{-2}, although each month is within the standard deviation of MERRA for the 1979-2005 period. As seen in equation (4), the MERRA energy tendency incorporates the cloud ice latent heating and kinetic energy terms which are not considered in other studies. For monthly means over the regions examined, however, these terms are negligible.

c. Energy convergence and transport

The divergence term in equation (3) is similarly composed of contributions from latent heat, virtual enthalpy, kinetic, and geopotential energy terms. For the north polar cap, the annual cycle of energy convergence from MERRA consists of values greater than 100 W m^{-2} during winter months September through March and a minimum of 72±10 W m^{-2} in May, as seen in Fig. 3(a). Porter et al. (2010) present annual cycles of energy convergence computed as a residual using several combinations of reanalyses and radiative flux data sets for the period 2000-2005, while Serreze et al. (2007) present ERA-40 and NCEP/NCAR reanalysis average monthly values for the period 1979-2001. While there is agreement of larger energy convergence in winter, there is considerable variability among the data sets on the months of the minimum and maximum value, with May providing a spread of 40 W m^{-2} among the various methods. MERRA values concurrent with these previous studies are found within this large range.

Figure 4(a) indicates that the average poleward energy transport across 70°N is zonally asymmetric and is focused at preferred longitudes which are associated with the mean longwave circulation patterns in the middle troposphere (Serreze et al., 2007). In comparison to energy transports across 70°N from ERA-40 as reported by Serreze et al. (2007), MERRA transports shown in Fig. 4(a) are comparable but with some differences. First, the poleward (positive) flux centered near 315°E (45°W) has a smaller zonal extent than is shown in Serreze et al. (2007). This may be due to the higher spatial resolution of MERRA and the role of the Greenland Ice Sheet topography in defining the mid-tropospheric trough pattern over eastern North America.

Second, the wintertime poleward transport near 150°E is shown in MERRA to be greater than $20 \cdot 10^9$ W m^{-1}. This is stronger by one contour level ($5 \cdot 10^9$ W m^{-1}) than that shown by Serreze et al. for ERA-40. But in general the average meridional transport patterns of MERRA and ERA-40 are remarkably similar.

In the Southern Hemisphere, prior studies on atmospheric energy convergence are not as recent. However comparisons to MERRA may be made using Nakamura and Oort (1988) and Genthon and Krinner (1998). Using GCM output, Nakamura and Oort (1988) estimated a mean annual energy convergence across 70°S of 95 W m^{-2}, which is 23 W m^{-2} less than shown for MERRA in Table 1. As seen in Fig. 3(b), the annual cycle in MERRA contains a broad maximum over winter months and a short period of minimum of values less than 100 W m^{-2} in December, January, and February. In contrast Nakamura and Oort (1988) indicate lower amounts in the autumn, and the annual cycle is generally more sinusoidal. Nakamura and Oort (1988) and MERRA monthly energy convergence values are comparable over the months June to October but differ by 45 W m^{-2} in January. More recently, Genthon and Krinner (1998) produced seasonal averages and zonal distributions of energy transport using the ERA-15 reanalysis for the period 1979-1993. The annual atmospheric energy convergence derived from ERA-15 of 81 W m^{-2} is considerably smaller than corresponding values of either MERRA or Nakamura and Oort (1988). Seasonally, the largest differences between MERRA and ERA-15 values from Genthon and Krinner (1998) are in autumn. Energy convergence for the south polar cap for March-April-May averages 134 W m^{-2} in MERRA, while Genthon and Krinner (1998) reported 79 W m^{-2}. The spatial distribution of energy transports along the 70°S parallel is strongly dependent on the meandering of the coastline, such that spatial resolution and topography are significant. Thus the differences between MERRA and ERA-15, though large, may partially result from differing model grids. Additionally, ERA-15 was known to employ a defective topography over the ice sheet. A visual inspection of Genthon and Krinner (1998) results indicates that the ERA-15 mean annual poleward transport is less than MERRA near 30°E, an intersection point between the 70°S parallel and the East Antarctic coastal escarpment. For this location, Genthon and Krinner (1998) plot amounts of between 2 and $3{\cdot}10^9$ W m^{-1} while MERRA values are greater than $5{\cdot}10^9$ W m^{-1}. Additionally Genthon and Krinner indicate an annual mean equatorward energy transport in the Ross Sea, while MERRA indicates a poleward flux. MERRA and ERA-15 share some general characteristics of the meridional energy transport including a seasonal change in the south Pacific region between 180°E and 270°E from poleward during winter months to equatorward in summer , as shown in Fig. 4(b). The figure also shows an opposing seasonal reversal between 270°E and 300°E in MERRA, and this is also reflected in Genthon and Krinner (1998).

d. TOA radiative fluxes

For the north polar cap, MERRA TOA radiative fluxes are compared to ERBE (Serreze et al., 2007) and measurements from CERES (Porter et al., 2010). With the exception of midsummer months, the Arctic TOA radiative flux in MERRA is mainly directed upwards ($R_{top} < 0$), with an annual average of –110±1 W m^{-2}. Annual estimates from ERBE and CERES are within the standard deviation of this value. On the monthly time scale, the largest differences are for the month of May, where the MERRA 1979-2005 value of –23±2 W m^{-2} compares with -53 W m^{-2} in ERBE and –37 W m^{-2} in CERES. Using MERRA averages concurrent with these satellite records, MERRA is less than satellite estimates for May by 29 W m^{-2} as compared to ERBE and by 12 W m^{-2} as compared to CERES. In July, CERES indicates a net downwards

TOA flux of 21 W m^{-2} compared to a 1 W m^{-2} upwards flux in MERRA, while ERBE and MERRA concurrent July values are equal. For other months, the differences are small.

For the south polar cap, the TOA net radiative flux remains negative throughout the year. Both the ERBE data and the values from Nakamura and Oort (1988) indicate that the annual net TOA radiative flux magnitude in MERRA is too large, and that the discrepancy is largest during winter months. The 1979-2005 average net flux as shown in Table 1 for MERRA is -101±1 W m^{-2}. This compares with –90 W m^{-2} from the historical satellite data used in Nakamura and Oort (1988), and –95 W m^{-2} from ERBE for the period February 1985 to April 1989 (Briegleb and Bromwich, 1998). The MERRA 1979-2005 annual average is by chance equal to the 1985-1989 time period. For the months of June, July, and August, the average flux from Nakamura and Oort (1988) is –131 W m^{-2}, and from ERBE, –134 W m^{-2}. For MERRA, the corresponding value is –142 W m^{-2} for both 1979-2005 and 1985-1989 time periods. In these winter months, the difference between MERRA and satellite values is almost entirely composed of the outgoing longwave component.

The time series of MERRA TOA radiative fluxes indicate potentially spurious trends in both polar regions. Over north and south polar caps, year to year variability in R_{top} resembles that of the energy budget IAU. For the north polar cap, a maximum for R_{top} is reached in 1993 with -107 W m^{-2}, with values as low as –112 W m^{-2} occurring in 1981 and 2005. MERRA TOA fluxes for the south polar cap have an irregular time series with a range between minimum and maximum values of 4 W m^{-2}. Over the Southern Ocean domain, a sharp change is noted after 1998. This is likely due to the introduction of AMSU data to the observing system as noted earlier. Annual average values prior to 1998 are consistent with an average of –81±1 W m^{-2}. For the period 1999-2005 the MERRA average for the Southern Ocean is –86±2 W m^{-2}.

e. Surface fluxes

Figure 5 shows the annual average surface net heat flux from MERRA for both polar regions. In the Northern Hemisphere, small negative values of between 0 and –5 W m^{-2} are found in a uniform field over nonglaciated land surfaces, which is consistent with subsurface warming in recent years (Serreze et al., 2007). Over the central Arctic Ocean, MERRA net surface flux values are positive as expected but are exceptionally large. Values greater than 15 W m^{-2} are found in the central Arctic, and greater than 20 W m^{-2} in the approaches to the North Atlantic. These annual values are extraordinary and likely not realistic. A comparison of the averaged annual time series of monthly values with previous studies indicates largest discrepancies occuring in summer months. The July 1979-2005 net surface flux for MERRA is -68 ± 4 W m^{-2} for the north polar cap as shown in Table 1. This compares with –85 W m^{-2} for ERA-40 (Serreze et al., 2007) and –86 W m^{-2} for JRA-25 (Porter et al., 2010).

The MERRA energy budget contains the surface heat flux resulting from solid precipitation which is generally not accounted for in other studies, however this contribution is small compared to the differences in net flux values. The solid precipitation term is largest over land surfaces. Solid precipitation latent heating averages 4.3±0.4 Wm^{-2} over Greenland and 2.3±0.1 W m^{-2} over the Arctic Ocean domain.

Discrepancies in the surface flux fields are evaluated using observations from the Surface Heat Budget of the Arctic ice camp field study in the Beaufort Sea in October 1997 to October 1998 (SHEBA; Uttal et al., 2002). MERRA surface flux values are compared with a compilation of observed radiative and turbulent flux measurements by Duynkerke and de Roode (2001). For this data source, SHEBA latent heat flux observations were limited and are not considered. Using the remaining energy budget components, a net flux comparison indicates a positive (upward) bias in MERRA of 18 W m^{-2} for the months October to April, –1 W m^{-2} for May, and small positive biases for the following summer months. There are three fundamental results of the comparison. As shown in Fig. 6, substantial differences in the upwelling shortwave radiative flux result from an overly simplistic representation of sea ice properties. Sea ice albedo is set to a fixed value of 0.60 for MERRA. The ice surface observed in SHEBA has a much higher albedo in springtime– monthly averages of 0.83 in March, April, and May, and 0.74 in June. This difference contributes to an underestimate in the upwelling shortwave flux of 55 W m^{-2} in April, 80 W m^{-2} in May, and 56 W m^{-2} in June. In late summer, the observed surface albedo is degraded by melting and becomes comparable to the MERRA value. In late autumn, freezing and the introduction of solid precipitation again produces surface albedo differences between MERRA and observation, however the incoming solar flux is reduced and the impact on the upwelling shortwave is less consequential. The difference with observation in the upwelling shortwave radiative flux for May is the largest of any monthly budget component.

The second result is a response in other MERRA surface energy budget terms in May to the albedo bias. Surface temperatures over ice in MERRA are determined via energy balance, and the underestimate of the surface albedo results in a perceived increased absorption of solar energy and a surface warming. This likely results in the springtime MERRA sensible heat flux bias, which is found to be 16 W m^{-2} in May. Other than the April, May, and June period, the MERRA sensible heat flux difference with SHEBA observations is only 2 W m^{-2}. An intriguing finding is a springtime negative bias with SHEBA observations in the downwelling shortwave radiative flux. The MERRA downwelling shortwave is underestimated by 36 W m^{-2} in April, 37 W m^{-2} in May and 25 W m^{-2} in June. In other months this difference is about 1 W m^{-2}. This bias is likely associated with general deficiencies in the representation of cloud properties. From the seasonal timing of the bias, however, it is speculated that a portion of the amount is due to a redistribution of cloudiness in the atmospheric column resulting from anomalous surface warming. The large May bias in upwelling shortwave radiation is then compensated for by biases in downwelling shortwave radiation and the sensible heat flux to produce the surface net energy flux bias of –1 W m^{-2}.

Shown in Fig. 7 is the time series of hourly near-surface air temperature in comparison to the observed time series from SHEBA for the period 1 February to 30 June,1998. A temperature bias in spring is readily apparent, with a difference of greater than 3.5°C in April and May before the freezing value is reached in early June. In particular, the period 19 April to 10 May shows an average bias of 6.1°C in MERRA. For daily averages, however, there is a good correlation between MERRA and observation for the period shown (r=0.95). It may be seen in the time series of hourly values shown Fig. 7 that the diurnal cycle in MERRA temperature has an amplitude between 2 and 10°C, which begins abruptly on 28 March and continues unabated until the freezing point is reached in June. The observed SHEBA diurnal cycle has a similar amplitude, however the cycle is not as regular as in MERRA and there are periods of considerable interruption, perhaps due to synoptic variability. These differences are suggestive of difficulties in MERRA boundary layer parameterizations. Springtime air temperature biases are found at Arctic station locations as well. For example, a comparison with Sachs Harbor (72°N, 125°W) over the period 1979-2005 indicates an average of 4.9°C difference for April but only 1.9°C for the months August through March. A comparison with Barrow (71°N, 157°W) similarly indicates an average bias in MERRA of 3.6°C for the spring months of March, April, and May and 0.9°C for other months. But as shown in Fig. 8, MERRA performs well in a comparison of monthly anomalies. The correlation between temperature anomalies at Barrow and Jan Mayan (71°N, 9°W) is 0.99 for both stations. The time series shown in Fig. 8 contain observations that cover the entire time period. Other stations in the Arctic with shorter and/or interrupted records compare similarly well.

The third result in the comparison with SHEBA is a negative bias in the downwelling longwave radiative flux throughout the year of 12 W m^{-2}. This quantity leads to the overall positive bias in the net surface flux for summer, autumn, and winter months. As with the springtime downwelling shortwave radiative flux bias, an inadequate representation of cloud properties is implied. To evaluate this further, comparisons were made between MERRA and SHEBA hourly microwave radiometer retrievals over the period 5 December 1997 to 9 September 1998. More than 5000 observations were made over the period. Retrievals of precipitable water compare remarkably well to MERRA values as seen in Fig. 9(a), although differences are apparent for small quantities in winter. For monthly intervals, the correlation between MERRA and the hourly microwave radiometer precipitable water retrievals ranges from r=0.87 in December 1997 to r=0.96 in May 1998. A consistent bias of 0.6±0.2 mm in monthly averages is found, which amounts to 31 percent of the observed average for January but only 3 percent for July. In contrast, the comparison to retrieved liquid water content shown in Fig. 9(b) is less favorable. Cloud liquid water from the SHEBA microwave radiometer ranges from an average of 0.017 mm in January 1997 to 0.106 mm in August 1998. Typical MERRA values are about 45 percent of the microwave radiometer amounts. Although large discrepancies have been noted between the SHEBA microwave radiometer values for liquid water path and simultaneous aircraft measurements (Lin et al., 2001), the differences between MERRA and SHEBA values exceed 50 percent. Additionally, the correlations of hourly liquid water path values with MERRA over monthly time intervals are low and range from r=0.14 in April 1998 to r=0.55 in January 1998. The presence or absence of cloud liquid water significantly alters the downwelling longwave radiative flux. An underestimate of cloud liquid water in MERRA is qualitatively consistent with differences in the surface net flux with observation.

Turning to the Southern Hemisphere, the annual average net surface heat flux for the south polar cap is shown in Fig. 5(b). Of immediate concern is the anomalous non-zero field over Antarctica, which is shared by the major ice sheets in both polar regions. Over grounded ice, the MERRA subsurface energy flux is determined in the GEOS-5 model by the prognostic temperature for a 7 cm (water-equivalent) surface ice layer and a "deep" layer temperature at 2 m depth that is fixed at 230°K. Thus location of the zero value contour in Fig. 5(b) exactly matches the annual averaged 230°K surface temperature isotherm. Observations from automatic weather stations indicate that annual mean subsurface conductive heat fluxes are not significant (e.g., Reijmer and Oerlemans, 2002), and annual surface energy flux patterns in MERRA over Antactica (as well as Greenland) are erroneous.

The pattern in the MERRA annual surface net energy flux in Antarctica is manifest as a complementary distribution of downward (negative) turbulent and upward (positive) radiative fluxes that are not balanced. MERRA annual mean latent heating exceeds 5 W m^{-2} only along the East Antarctic coast in selected locations, and averages less than 1 W m^{-2} for the total grounded ice sheet area. The annual averaged sensible heat flux over the ice sheet is uniformly negative and is approximately contour-parallel with topography, with magnitudes greater than (-) 60 W m^{-2} along the East Antarctic coastal escarpment decreasing to less than (–) 10 W m^{-2} over the central plateau. The annual mean net radiative flux field in MERRA is spatially more uniform with values ranging from (+)25 to 35 W m^{-2} for East Antarctica, and smaller positive values over West Antarctica. This results in the imbalances in the net surface heat flux as shown. Over the interior plateau, net flux values are as large as +15 W m^{-2} while the net amounts at lower elevations are negative and are less than –30 W m^{-2} over the East Antarctic coastal escarpment. These errors in the net surface flux have relation to near-surface temperature biases. As shown in Fig. 10, there is a considerable wintertime warm bias of 5°C at Amundsen-Scott (90°S), while a summer cold bias of 5°C is found at Scott Base (78°S, 167°E). Visual comparison with satellite-derived surface air temperatures in Comiso (2000) indicates that the summer cold bias extends over the embayment regions.

Comparisons of surface energy budget components are made with Antarctic station values compiled by King and Turner (1997). Values compiled by King and Turner (1997) reflect studies of opportunity and do not account for interannual variability. This may be partially compensated for by noting the variability in the 1979-2005 MERRA record. For the sensible heat flux, MERRA averages at Mizuho (71°S, 44°E) of –47±8 W m^{-2} in July and –19±4 W m^{-2} in December compare with observational values of –37 and –25 W m^{-2} for July and December, respectively (Ohata et al., 1985). At South Pole, differences in seasonal values of the sensible heat flux are largest in spring and summer. The December-January-February sensible flux average from MERRA is –3±1 W m^{-2} and –22 W m^{-2} in observation (Carroll, 1982). This contributes to a difference of 9 W m^{-2} in the annual average.

Large differences from observation are also associated with the net radiative flux. At Halley (76°S, 26°W), the annual average net radiative flux for MERRA of 13±3 W m^{-2} approximates the observational values of 9.8 W m^{-2}, however seasonal differences are as large as 10 W m^{-2} in winter. At South Pole, the annual net radiative flux of 19±1 W m^{-2} matches the observation of Carroll (1982), however seasonal differences are large. In winter, the net radiative surface cooling of 36±2 W m^{-2} exceeds the observed value of 21 W m^{-2}. In summer, the MERRA radiative flux value of –7±1 W m^{-2} differs from the Carroll (1982) value of +18 W m^{-2}.

The surface radiative flux differences at South Pole are examined using the observations of Dutton et al. (1989), who recorded daily mean radiative flux components from April 1986 until February 1988. Over this period, the surface net radiative flux for both MERRA and observation is positive for most of the year but becomes negative in summer months as seen in Fig. 11. Over the 22 month period, the downwelling longwave radiative flux is consistently less than observation by an average 24±6 W m^{-2}. This difference is apparent in the comparison of daily values in Fig. 11. Large biases are also found in the MERRA net shortwave radiative flux in spring and summer. For the month of January, the net downward shortwave flux is overestimated by 20 W m^{-2} in 1987, and by 23 W m^{-2} in 1988. A minor part of the shortwave bias is associated with the MERRA surface albedo, which is fixed over land ice at 0.775. Observed monthly averages at South Pole indicate an albedo of between 0.80 and 0.89. These differences in the shortwave flux partially cancel the downwelling longwave underestimate in summer. It may be seen from Fig. 11 that some of the day-to-day variability in the downwelling longwave radiative flux is reproduced in MERRA. By subtracting a 30-day running mean from each time series to remove the annual cycle, the two curves have a correlation of 0.70.

The annual cycle of the net surface flux for the Southern Ocean is shown in Fig. 3(c). Using ECMWF operational analyses overlapping the period of the ERBE study, Okada and Yamanouchi (2002) examined the atmospheric energy budget for the region bounded by 60°S and 70°S. Okada and Yamanouchi estimated the surface energy budget as the residual using TOA ERBE radiation and analyses divergence terms. A seasonal asymmetry in the net surface flux was highlighted, which was found to abruptly peak in May with a maximum value of

116 W m^{-2}. Okada and Yamanouchi (2002) attributed this asymmetry to the latent heat release resulting from sea ice formation. As seen in Fig. 3(c), the MERRA surface energy flux over the Southern Ocean sea ice domain is also asymmetric and peaks in May at 98±4 W m^{-2}, however the maximum is not as striking as was found for the ECMWF analyses. In examining the autumnal surface turbulent fluxes in MERRA, it is found that the total latent heat flux is a maximum for the domain in April with 33 W m^{-2}. The latent heat flux then diminished over ice covered winter months, with a second maxima in November of 28 W m^{-2}. The MERRA sensible heat flux reaches its annual maximum in May of 21 W m^{-2} and generally reflects the shape of surface net flux. The asymmetry in the annual cycle for the MERRA net surface flux as shown in Fig. 3(c) is principally due to seasonal changes in the sensible heat flux. In reanalyses, sea ice cover is prescribed from observational fields. The latent heat flux arising from ice formation is manifest as the net conductive flux at the atmosphere-ice interface. In this context, MERRA and the results of Okada and Yamanouchi (2002) are broadly consistent.

4. Summary and Discussion

MERRA reproduces the basic patterns of energy flow in the polar atmosphere as they are known. As shown in Fig. 3, the polar regions are marked by a convergence of energy from lower latitudes for all months, and a loss of energy at the top of the atmosphere for the most of the year. In the Arctic, reductions in the TOA shortwave radiative flux in autumn produce a negative tendency in the atmospheric column total energy throughout the period August through January, which is moderated by contributions from the net surface flux and increased energy transport from lower latitudes in winter (Serreze et al., 2007). In the Antarctic, this seasonal progression is less sinusoidal, with the net TOA radiative flux remaining negative throughout the year, and an extended winter period in the energy budget components extending from April to September.

Despite reproducing these essential components, MERRA energy budgets for the Arctic and Antarctic contain substantial errors owing to overly simplistic physical parameterizations, including sea ice albedo, the surface heat budget over permanent land ice, and cloud radiative properties. Difficulties in MERRA with sea ice characteristics are not dissimilar from those described in Bretherton et al. (2000) for ECMWF analyses produced during SHEBA, and indeed the discrepancies in surface shortwave radiative fluxes are similar. Spring is a critical period for evaluation of surface flux fields in the Arctic, and differences between MERRA shortwave surface radiative fluxes with observation are most prominent in May. Over the data sparse Southern Ocean, discontinuities in the time series of TOA radiative fluxes coincide with the introduction of AMSU satellite data in November 1998 and are therefore spurious. Elsewhere, interannual variability of the IAU budget adjustment quantity is large but not as easily linked to changes in the observing system. Additional characterization of IAU variables, including their vertical distribution, and MERRA cloud properties are conspicuous points for further evaluation.

MERRA nevertheless compares favorably to previous studies of energy budget components produced from state and dynamical variables. Atmospheric energy convergence and the spatial distribution of transport along the 70° parallel compare closely with previous studies in the Northern Hemisphere, while estimates for the south polar cap are qualitatively similar but may also been seen as an update to studies based on earlier analyses. The total atmospheric energy tendency in polar regions also compares favorably to previous studies.

Credible estimates of the atmospheric energy budget in polar regions continue to be a significant challenge due to changes in the observing system and complex energy feedback mechanisms that are associated with the high latitudes. Evaluation using both representative point location observations and previous area-averaged estimates such as those used in this study are valuable for providing a straightforward appraisal of new reanalyses. The MERRA system is an important product due to its alternative construction, including a non-spectral background model and its emphasis on NASA satellite products. An important concept used in MERRA is the employment of the incremental analysis update, or IAU, for identifying differences between observations and the background analysis system. Inconsistencies in atmospheric budgets are quantified in the IAU, which is one means of measuring uncertainty.

A general criticism of reanalyses is that they are produced with the intent of providing the best representation of conditions for a given time without consideration for the impact of heterogeneous observations on temporal variability (Thorne and Vose, 2010). This intent nevertheless has practical, scientific application. Additionally, reanalyses may be seen as part of a spectrum of products for climate study ranging from heterogeneous observations to model simulations, which include AMIP fields and sparse data reanalyses (e.g., Compo et al., 2006). As part of that continuum, the IAU in MERRA provides a quantification of differences between observations and the background system. Changes in the spatial and temporal variability of the IAU imply changes to the observing system, which should be carefully treated in evaluating time series. MERRA is a valuable record for examining the polar atmosphere when these cautions are exercised.

Acknowledgments. Data from the Surface Heat Budget of the Arctic Ocean experiment (SHEBA) were obtained from the University of Washington Department of Atmospheric

Sciences, Seattle, Washington. Reference Antarctic Data for Environmental Research (READER) is a project of the Scientific Committee on Antarctic Research (SCAR) and were obtained from British Antarctic Survey (BAS), Cambridge, United Kingdom. Arctic station values from the Integrated Surface Database (ISD) and the Integrated Rawinsonde Global Rawinsonde Archive (IGRA) were obtained from the National Climate Data Center, Asheville, North Carolina. This study was funded by grants from the NASA Modeling Analysis and Prediction Program (MAP) and the NASA Energy and Water cycle Study (NEWS) to the second author.

APPENDIX

Representation of the Atmospheric Energy Budget Using MERRA Variables

The following MERRA variables are defined as follows:

DQVDT_DYN	Vertically integrated water vapor tendency for dynamics	kg m^{-2} s^{-1}
DQVDT_PHY	Vertically integrated water vapor tendency for physics	kg m^{-2} s^{-1}
DQVDT_ANA	Vertically integrated water vapor tendency for analysis	kg m^{-2} s^{-1}
DQLDT_DYN	Vertically integrated liquid water tendency for dynamics	kg m^{-2} s^{-1}
DQLDT_PHY	Vertically integrated liquid water tendency for physics	kg m^{-2} s^{-1}
DQLDT_ANA	Vertically integrated liquid water tendency for analysis	kg m^{-2} s^{-1}
DQIDT_DYN	Vertically integrated ice water tendency for dynamics	kg m^{-2} s^{-1}
DQIDT_PHY	Vertically integrated ice water tendency for physics	kg m^{-2} s^{-1}
DQIDT_ANA	Vertically integrated ice water tendency for analysis	kg m^{-2} s^{-1}
EVAP	Surface evaporation	kg m^{-2} s^{-1}
PRECTOT	Total surface precipitation flux	kg m^{-2} s^{-1}
DQVDT_CHM	Vertically integrated water tendency for chemistry	kg m^{-2} s^{-1}
DQVDT_FIL	Artificial “filling” of water vapor	kg m^{-2} s^{-1}
DQLDT_FIL	Artificial “filling” of liquid water	kg m^{-2} s^{-1}
DQIDT_FIL	Artificial “filling” of frozen water	kg m^{-2} s^{-1}

A tendency may be expressed as the sum of dynamics, physics, and analysis variables. For example, the tendency of vertically integrated water vapor (precipitable water) is expressed using MERRA variables as follows.

$$\frac{\partial W_{(v)}}{\partial t} := DQVDT\_DYN + DQVDT\_PHY + DQVDT\_ANA \qquad (8)$$

The analysis incremental update (IAU) is expressed by the "*_ANA*" variables. For atmospheric moisture, convergence is expressed by the dynamics variables. Equation (1) may then be written using MERRA variables as follows.

$$\begin{aligned}
&(DQVDT_DYN + DQVDT_PHY + DQVDT_ANA \\
&\quad + DQLDT_DYN + DQLDT_PHY + DQLDT_ANA \\
&\quad + DQIDT_DYN + DQIDT_PHY + DQIDT_ANA) \\
&\quad - (DQVDT_DYN + DQLDT_DYN + DQIDT_DYN) \\
&= EVAP - PRECTOT + DQVDT_CHM + \\
&\quad (DQVDT_FIL + DQLDT_FIL + DQIDT_FIL) \\
&\quad + (DQVDT_ANA + DQLDT_ANA + DQIDT_ANA) \qquad (9)
\end{aligned}$$

The following MERRA variables related to energetics are given as follows.

DKDT_DYN	Vertically integrated kinetic energy tendency for dynamics	W m^{-2}
DKDT_PHY	Vertically integrated kinetic energy tendency for physics	W m^{-2}
DKDT_ANA	Vertically integrated kinetic energy tendency for analysis	W m^{-2}
DHDT_DYN	Vertically integrated $c_P \cdot T_v$ tendency for dynamics	W m^{-2}
DHDT_PHY	Vertically integrated $c_P \cdot T_v$ tendency for physics	W m^{-2}
DHDT_ANA	Vertically integrated $c_P \cdot T_v$ tendency for analysis	W m^{-2}
DPDT_DYN	Potential energy tendency for dynamics	W m^{-2}
DPDT_PHY	Potential energy tendency for physics	W m^{-2}
DPDT_ANA	Potential energy tendency for analysis	W m^{-2}
CONVKE	Vertically integrated convergence of kinetic energy	W m^{-2}
CONVCPT	Vertically integrated convergence of virtual enthalpy	W m^{-2}
CONVPHI	Vertically integrated convergence of geopotential	W m^{-2}
SWTNT	TOA outgoing shortwave flux	W m^{-2}
SWGNT	Surface net downward shortwave flux	W m^{-2}
LWTUP	Upward TOA longwave flux	W m^{-2}
LWGNT	Net downward longwave flux at the surface	W m^{-2}
EFLUX	Latent heat flux (positive upward)	W m^{-2}
HFLUX	Sensible heat flux (positive upward)	W m^{-2}
PRECSN	Frozen precipitation at the surface	kg m^{-2} s^{-1}
DKDT_GEN	Generation of kinetic energy	W m^{-2}

TEFIXER	Total energy added by artificial energy "fixer"	W m^{-2}

As noted previously, the contribution of spurious residuals in the energy term is computed as the net difference between local contributions and the global mean. Following Suarez et al. (2010), this contribution may be represented as:

$$
\begin{aligned}
Q_{NUM} := &-DKDT\_DYN + CONVKE + CONVPHI \\
&+ DKDT\_GEN - DPDT\_DYN - TEFIXER
\end{aligned}
\tag{10}
$$

Equation (4) is represented as follows.

$$
\begin{aligned}
\frac{\partial A_E}{\partial t} := &\ L_v \cdot (DQVDT\_DYN + DQVDT\_PHY + DQVDT\_ANA) \\
&- L_f \cdot (DQIDT\_DYN + DQIDT\_PHY + DQIDT\_ANA) \\
&+ DHDT\_DYN + DHDT\_PHY + DHDT\_ANA \\
&+ DPDT\_DYN + DPDT\_PHY + DPDT\_ANA \\
&+ DKDT\_DYN + DKDT\_PHY + DKDT\_ANA
\end{aligned}
\tag{11}
$$

Equation (5) is represented as:

$$
\begin{aligned}
\nabla \cdot \widetilde{\mathbf{F}}_A := &-(L_v \cdot DQVDT\_DYN - L_f \cdot DQIDT\_DYN \\
&+ CONVKE + CONVCPT + CONVPHI)
\end{aligned}
\tag{12}
$$

Equations (6) and (7) are represented as follows.

$$
\begin{aligned}
R_{top} + F_{sfc} := &\ (SWTNT - LWTUP) - (SWGNT + LWGNT) \\
&+ EFLUX + HFLUX + L_f \cdot PRECSN
\end{aligned}
\tag{13}
$$

The remainder of equation (3) is given as follows.

$$
\begin{aligned}
&L_v \frac{\partial W_v}{\partial t}\bigg|_{CHM} + \left[L_v \frac{\partial W_v}{\partial t} - L_f \frac{\partial W_i}{\partial t} \right]_{FIL} + \varepsilon_{IAU(E)} := \\
&\quad L_v \cdot DQVDT\_CHM + (L_v \cdot DQVDT\_FIL - L_f \cdot DQIDT\_FIL) \\
&\quad + (L_v \cdot DQVDT\_ANA - L_f \cdot DQIDT\_ANA + DHDT\_ANA \\
&\quad + DKDT\_ANA + DPDT\_ANA)
\end{aligned}
\tag{14}
$$

REFERENCES

Barkstrom, B.R., 1984: The Earth Radiation Budget Experiment (ERBE). *Bull. Amer. Meteor. Soc.*, **65**, 1170-1185.

Bloom, S., L. Takacs, A. DaSilva, and D. Ledvina, 1996: Data assimilation using incremental analysis updates. *Mon. Wea. Rev.*, **124**, 1256-1271.

Bretherton, C.S., S.R. de Roode, C. Jakob, E.L. Andreas, J. Intrieri, and R.E. Moritz, and P.O.G. Persson, 2000: A comparison of the ECMWF forecast model with observations over the annual cycle at SHEBA. Unpublished manuscript, 46 pp. (Available from http://citeseerx.ist.psu.edu/viewdoc/download?doi=10.1.1.36.9608&rep=rep1&type=pdf).

Briegleb, B.P, and D.H. Bromwich, 1998: Polar climate simulations of the NCAR CCM3. *J. Climate*, 11, 1270-1286.

Carroll, J.J., 1982: Long-term means and short-term variability of the surface energy balance components at South Pole. *J. Geophys. Res.*, **87**, 4277-4286.

Comiso, J.C., 2000: Variability and trends in Antarctic surface temperatures from in situ and satellite infrared measurements. *J. Climate*, **13**, 1674-1696.

Compo, G.P., J.S. Whitaker, and P.D. Sardeshmukh, 2006: Feasibility of a 100-year reanalysis using only surface pressure data. *Bull. Amer. Meteor. Soc.*, **87**, 175-190.

Cullather, R.I., and M.G. Bosilovich, 2010: The moisture budget of the polar atmosphere in MERRA. *J. Climate*, submitted.

Duynkerke, P., and S. de Roode, 2001: Surface energy balance and turbulence characteristics observed at the SHEBA Ice Camp during FIRE III. *J. Geophys. Res.*, **106**, 15313-15322.

Dutton, E.G., R.S. Stone, J.J. DeLuisi, 1989: South Pole surface radiation balance measurements, April 1986 to February 1988. *NOAA ERL Air Resources Laboratory Data Report Series*, **17**, 49 pp.

Fasullo, J.T., and K.E. Trenberth, 2008: The annual cycle of the energy budget. Part I. Global mean and land–ocean exchanges. *J. Climate*, **21**, 2297-2312.

Genthon, C., and G. Krinner, 1998: Convergence and disposal of energy and moisture on the Antarctic polar cap from ECMWF Reanalyses and Forecasts. *J. Climate*, **11**, 1703-1716.

Gibson, J.K., P. Kållberg, S. Uppala, A. Hernandez, A. Nomura, and E. Serrano, 1997: *ERA Description*. ECMWF Reanalyis Project Report Series, No. 1, 72 pp.

Kalnay, E., M. Kanamitsu, R. Kistler, W. Collins, D. Deaven, L. Gandin, M. Iredell, S. Saha, G. White, J. Woollen, Y. Zhu, A. Leetmaa, R. Reynolds, M. Chelliah, W. Ebisuzaki, W.Higgins, J. Janowiak, K. C. Mo, C. Ropelewski, J. Wang, R. Jenne, and D. Joseph, 1996: The NCEP/NCAR 40-Year Reanalysis Project. *Bull. Amer. Meteorol. Soc.*, **77**, 437-472.

King, J.C., and J. Turner, 1997: *Antarctic Meteorology and Climatology*. Cambridge Univ. Press, United Kingdom, 409 pp.

Koster, R.D., M.J. Suárez, A. Ducharne, M. Stieglitz, and P. Kumar, 2000: A catchment-based approach to modeling land surface processes in a GCM, Part 1, Model Structure. *J. Geophys. Res.*, **105**, 24809-24822.

Levitus, S., 1984: Annual cycle of temperature and heat storage in the world ocean. *J. Phys. Ocean.*, **14**, 727-746.

Moody, E.G., M.D. King, S. Platnick, C.B. Schaaf, and F. Gao, 2005: Spatially complete global spectral surface albedos: Value-added datasets derived from Terra MODIS land products. *IEEE Trans. Geosci. Remote Sens.*, **43**, 144–158.

Nakamura, N., and A.H. Oort, 1988: Atmospheric heat budgets of the polar regions. *J. Geophys. Res.*, **93**, 9510-9524.

Ohata, T., N. Ishikawa, S. Kobayashi, and S. Kawaguchi, 1985: Heat balance at the snow surface in a katabatic wind zone, East Antarctica. *Ann. Glaciol.*, **6**, 174-177.

Okada, I., and T. Yamanouchi, 2002: Seasonal change of the atmospheric heat budget over the Southern Ocean from ECMWF and ERBE data. *J. Climate*, **15**, 2527-2536.

Porter, D.F., J.J. Cassano, M.C. Serreze, and D.N. Kindig, 2010: New estimates of the large-scale Arctic atmosphere energy budget. *J. Geophys. Res.*, **115**, D08108, doi:10.1029/2009JD012653.

Randall, D., J. Curry, D. Battisti, G. Flato, R. Grumbine, S. Hakkinen, D. Martinson, R. Preller, J. Walsh, and J. Weatherly, 1998: Status of and outlook for large-scale modeling of atmosphere–ice–ocean interactions in the Arctic. *Bull. Amer. Meteor. Soc.*, **79**, 197-219.

Reijmer, C.H., and J. Oerlemans, 2002: Temporal and spatial variability of the surface energy balance in Dronning Maud Land, East Antarctica. *J. Geophys. Res.*, **107**, 4759, doi:10.1029/2000JD000110.

Reynolds, R.W., N.A. Rayner, T.M. Smith, D.C. Stokes, and W. Wang, 2002: An improved in situ and satellite SST analysis for climate. *J. Climate*, **15**, 1609–1625.

Rienecker, M.M., M.J. Suarez, R. Todling, J. Bacmeister, L. Takacs, H.-C. Liu, W. Gu, M. Sienkiewicz, R.D. Koster, R. Gelaro, I. Stajner, and E. Nielsen, 2009: *The GEOS-5 Data Assimilation System- Documentation of Versions 5.0.1, 5.1.0, and 5.2.0*. Technical Report Series on Global Modeling and Data Assimilation, NASA/TM-2007-104606, M.J. Suarez, Ed., Vol. 27, 95 pp.

Rienecker, M.M., and coauthors, 2010: The NASA Modern Era Retrospective-Analysis for Research and Applications (MERRA). *J. Climate* (in preparation).

Saha, S., S. Moorthi, H.-L. Pan, X. Wu, J. Wang, S. Nadiga, P. Tripp, R. Kistler, J. Woollen, D. Behringer, H. Liu, D. Stokes, R. Grumbine, G. Gayno, J. Wang, Y.-T. Hou, H. Chuang, H.H. Juang, J. Sela, M. Iredell, R. Treadon, D. Kleist, P. Van Delst, D. Keyser, J. Derber, M. Ek, J. Meng, H. Wei, R. Yang, S. Lord, H. van den Dool, A. Kumar, W. Wang, C. Long, M. Chelliah, Y. Xue, B. Huang, J.-K. Schemm, W. Ebisuzaki, R. Lin, P. Xie, M. Chen, S. Zhou, W. Higgins, C.-Z. Zou, Q. Liu, Y. Chen, Y. Han, L. Cucurull, R.W. Reynolds, G. Rutledge, and M. Goldberg, 2010: The NCEP Climate Forecast System Reanalysis. *Bull. Amer. Meteor. Soc.*, submitted.

Serreze, M.C., A.P. Barrett, A.G. Slater, M. Steele, J. Zhang, and K.E. Trenberth, 2007: The large-scale energy budget of the Arctic. *J. Geophys. Res.*, **112**, D11122, doi:10.1029/2006JD008230.

Stieglitz, M., A. Ducharne, R.D. Koster, and M.J. Suarez, 2001: The impact of detailed snow physics on the simulation of snow cover and subsurface thermodynamics at continental scales. *J. Hydrometeorol.*, **2**, 228-242.

Suarez, M.J., and coauthor, 2010: *File Specification for MERRA Gridded Output*. Version 2.1. Global Modeling and Assimilation Office, National Aeronautics and Space Administration, Greenbelt, MD., 96 pp. (Available from: http://gmao.gsfc.nasa.gov/research/merra/file_specifications.php).

Thorne, P.W., and R.S. Vose, 2010: Reanalyses suitable for characterizing long-term trends. Are they really achievable? *Bull. Amer. Meteor. Soc.*, **91**, 353-361.

Trenberth, K.E., 1997: Using atmospheric budgets as a constraint on surface fluxes. *J. Climate*, **10**, 2796-2809.

Uppala, S.M., P.W. Kållberg, A.J. Simmons, U. Andrae, V. da Costa Bechtold, M. Fiorino, J.K. Gibson, J. Haseler, A. Hernandez, G.A. Kelly, X. Li, K. Onogi, S. Saarinen, N. Sokka, R.P. Allan, E. Andersson, K. Arpe, M.A. Balmaseda, A.C.M. Beljaars, L. van de Berg, J. Bidlot, N. Bormann, S. Caires, F. Chevallier, A. Dethof, M. Dragosavac, M. Fisher, M. Fuentes, S. Hagemann, E. Hólm, B.J. Hoskins, L. Isaksen, P.A.E.M. Janssen, R. Jenne, A.P. McNally, J.-F. Mahfouf, J.-J. Morcrette, N.A. Rayner, R.W. Saunders, P. Simon, A. Sterl, K.E. Trenberth, A. Untch, D. Vasiljevic, P. Viterbo, and J. Woollen, 2005: The ERA-40 re-analysis. *Quart. J. R. Meteorol. Soc.*, **131**, 2961-3012.

Uttal, T., J.A. Curry, M.G. Mcphee, D.K. Perovich, R.E. Moritz, J.A. Maslanik, P.S. Guest, H.L. Stern, J.A. Moore, R. Turenne, A. Heiberg, M.C. Serreze, D.P. Wylie, O.G. Persson, C.A. Paulson, C. Halle, J.H. Morison, P.A. Wheeler, A. Makshtas, H. Welch, M.D. Shupe, J.M. Intrieri, K. Stamnes, R.W. Lindsey, R. Pinkel, W.S. Pegau, T.P. Stanton, and T.C. Grenfeld, 2002: Surface Heat Budget of the Arctic Ocean. *Bull. Amer. Meteor. Soc.*, **83**, 255–275.

Wielicki, B.A., B.R. Barkstrom, E.F. Harrison, R.B. Lee, G.L. Smith, and J.E. Cooper, 1996: Clouds and the Earth's Radiant Energy System (CERES): An Earth Observing System experiment. *Bull. Amer. Meteor. Soc.*, **77**, 853-868.

TABLE 1. Components of the MERRA atmospheric energy budget for regions defined in Fig. 1, in W m^{-2}. The surface flux F_{sfc} discounts latent heating from solid precipitation. Uncertainty is indicated with the standard deviation over the 1979-2005 time period.

		$\partial A_E / \partial t$	$-\nabla \cdot F_A$	R_{top}	F_{sfc}	$\varepsilon_{IAU(E)} - Q_{NUM}$
70°N – 90°N	January	–1 ± 11	110 ± 16	–173 ± 4	63 ± 5	–5 ± 9
	July	2 ± 6	81 ± 8	2 ± 3	–68 ± 4	–13 ± 5
	Mean	0 ± 2	99 ± 4	–110 ± 1	19 ± 1	–11 ± 5
Arctic Ocean	January	–3 ± 13	106 ± 19	–176 ± 4	70 ± 5	–5 ± 14
	July	3 ± 9	96 ± 10	–7 ± 4	–75 ± 6	–9 ± 6
	Mean	0 ± 2	99 ± 6	–114 ± 1	23 ± 2	–9 ± 7
Greenland	January	–2 ± 19	143 ± 26	–153 ± 6	–1 ± 4	4 ± 16
	July	1 ± 8	118 ± 19	–48 ± 1	–40 ± 1	–32 ± 16
	Mean	0 ± 2	138 ± 9	–112 ± 1	–16 ± 1	–14 ± 9
70°S – 90°S	January	–1 ± 10	78 ± 10	–25 ± 2	–32 ± 2	–23 ± 8
	July	–10 ± 13	131 ± 16	–142 ± 3	19 ± 2	–21 ± 10
	Mean	0 ± 1	118 ± 6	–101 ± 1	3 ± 1	–22 ± 6
Southern Ocean	January	2 ± 6	97 ± 17	58 ± 10	–114 ± 9	–40 ± 17
	July	–7 ± 8	91 ± 15	–174 ± 1	82 ± 3	–11 ± 13
	Mean	0 ± 1	89 ± 5	–83 ± 2	12 ± 2	–23 ± 5
Antarctica	January	–2 ± 10	80 ± 11	–41 ± 1	–21 ± 1	–21 ± 8
	July	–9 ± 12	135 ± 18	–134 ± 3	7 ± 2	–20 ± 10
	Mean	0 ± 1	124 ± 5	–101 ± 1	–3 ± 1	–23 ± 5

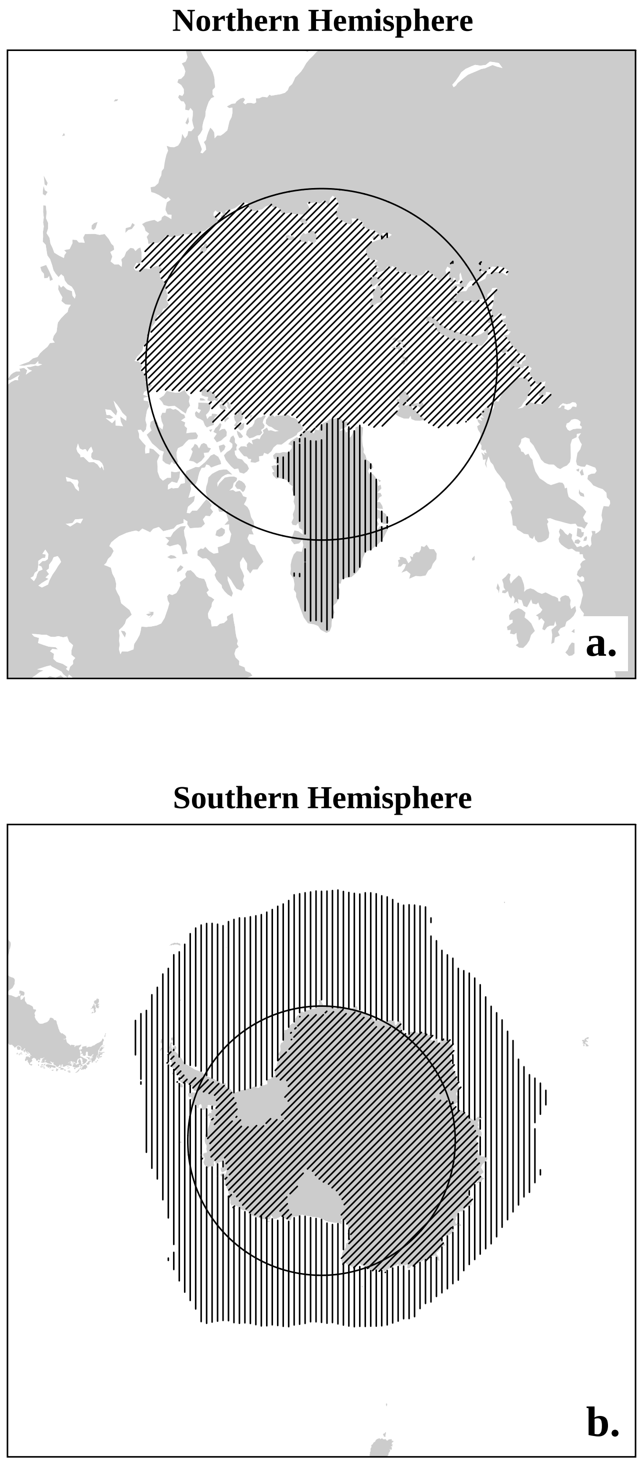

FIGURE 1. Regions of study for (a.) the Northern Hemisphere and (b.) the Southern Hemisphere. Bold line indicates the 70° parallel. Continental areas are shaded gray.

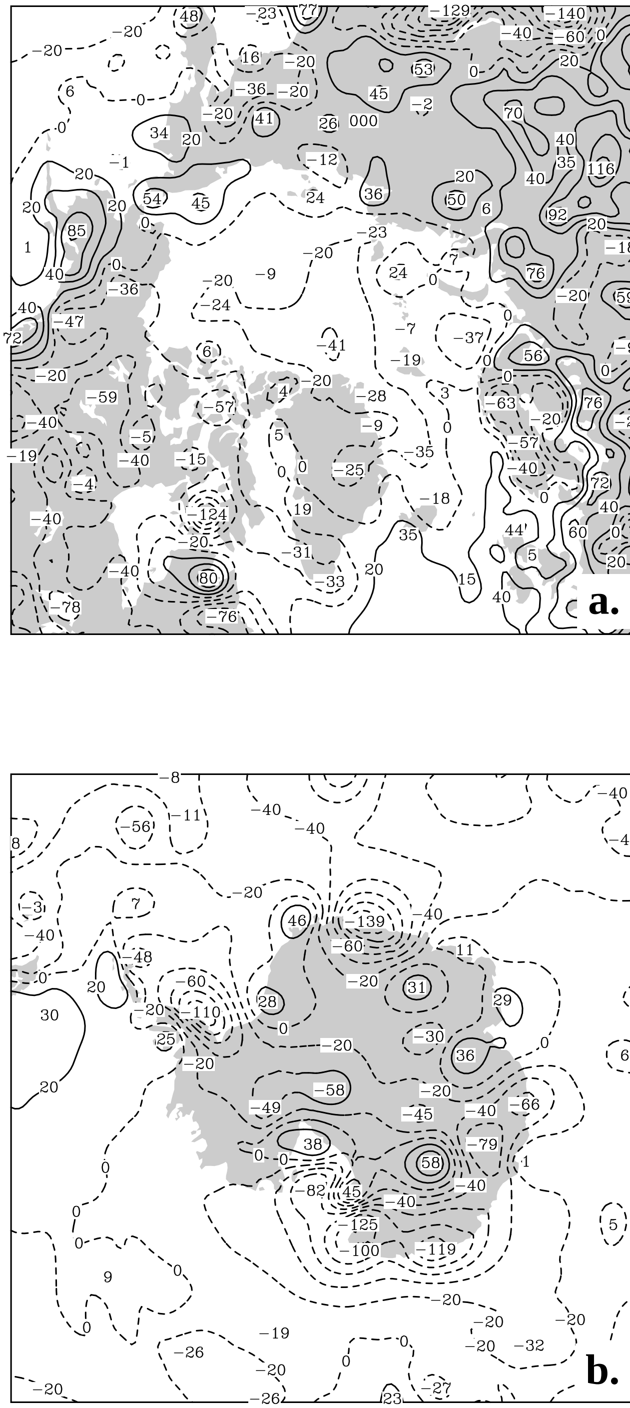

FIGURE 2. Average MERRA analysis incremental update field for the atmospheric energy budget for (a.) the Northern Hemisphere and (b.) the Southern Hemisphere. The contour interval is 20 W m^{-2}.

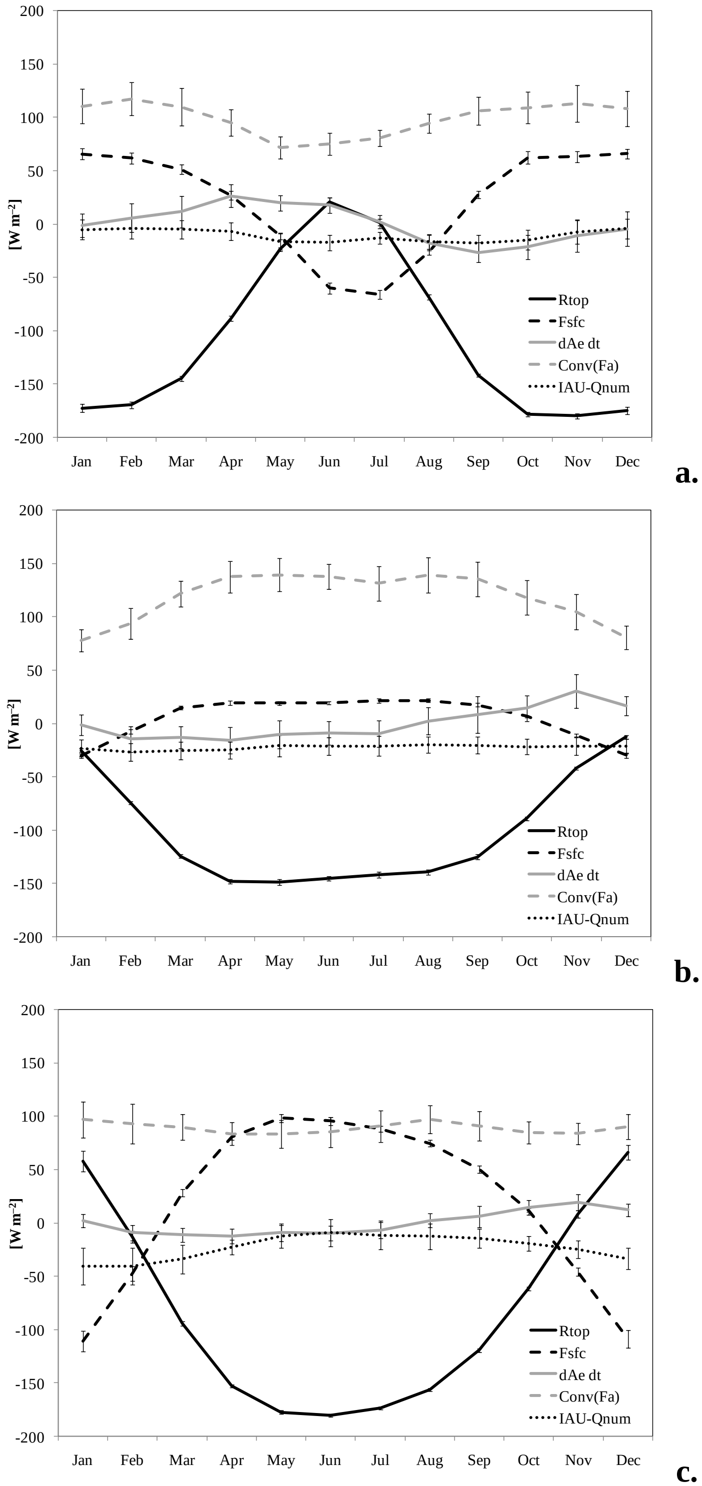

FIGURE 3. Annual cycle of atmospheric energy budget components in MERRA for (a.) north polar cap, (b.) south polar cap, and (c.) the Southern Ocean domain, in W m-2. Bars indicate plus and minus the standard deviation for the period 1979-2005.

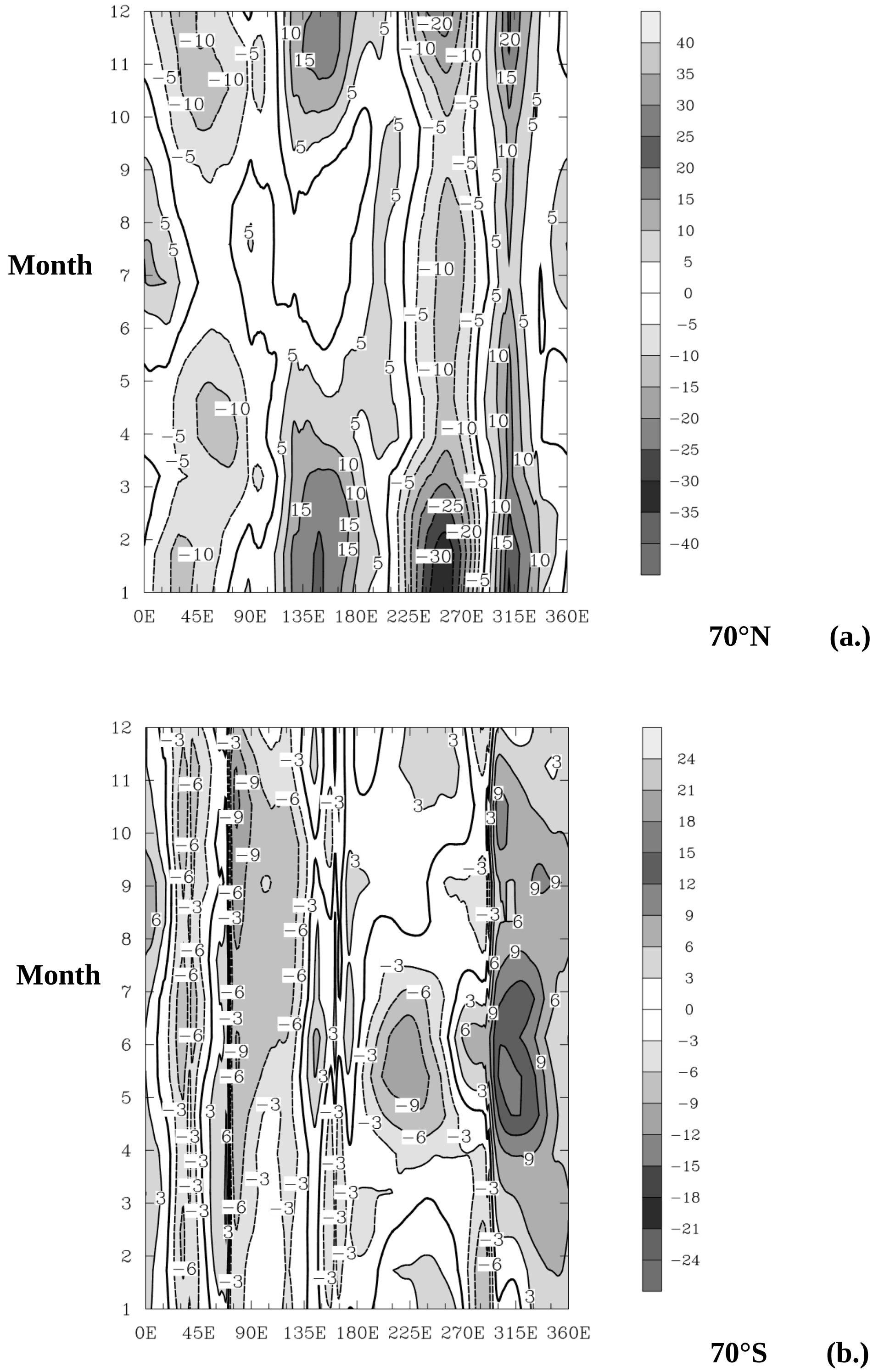

FIGURE 4. Average monthly meridional energy transport from MERRA (a.) across 70°N, contoured every $5{\cdot}10^9$ W m^{-1}, and (b.) 70°S, contoured every $3{\cdot}10^9$ W m^{-1}. Positive values indicate northward transport.

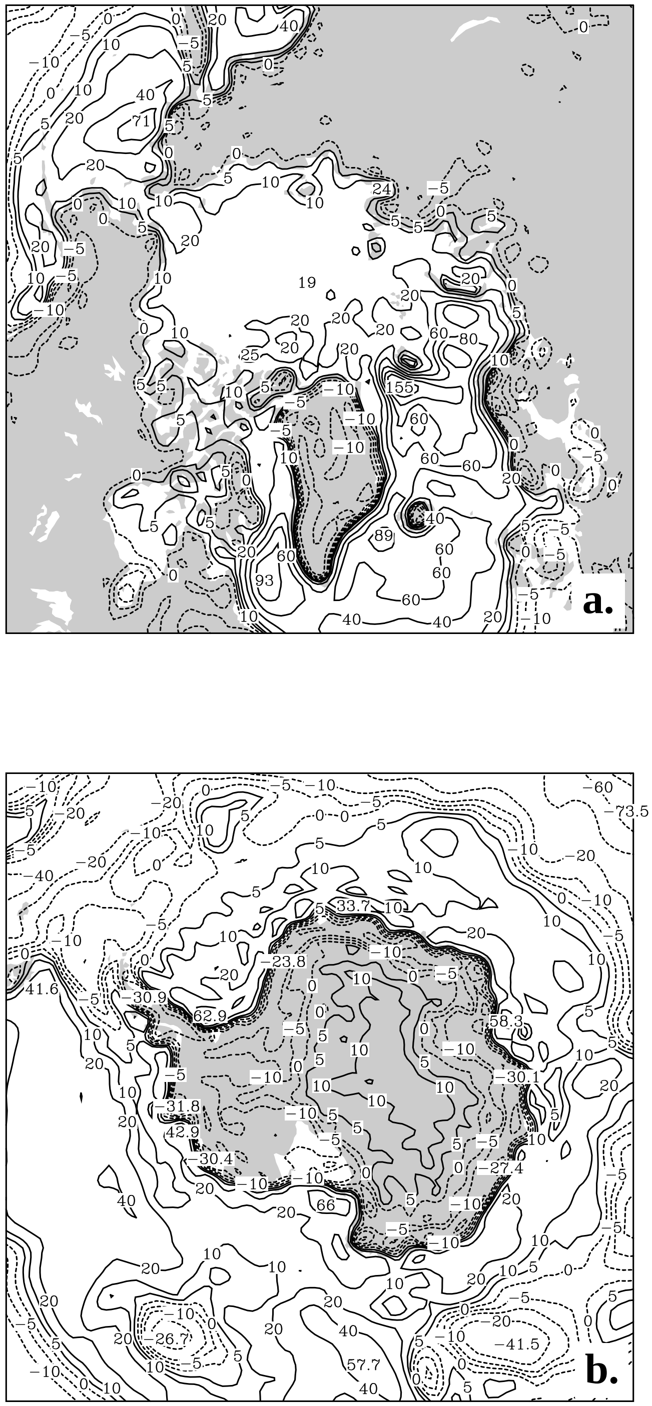

FIGURE 5. Annual average surface heat flux. The fields have been smoothed using a simple nine-point weighted algorithm. Contours are plotted with an interval of 20 W m^{-2} and for the levels –10, –5, 0, 5, and 10 W m^{-2}.

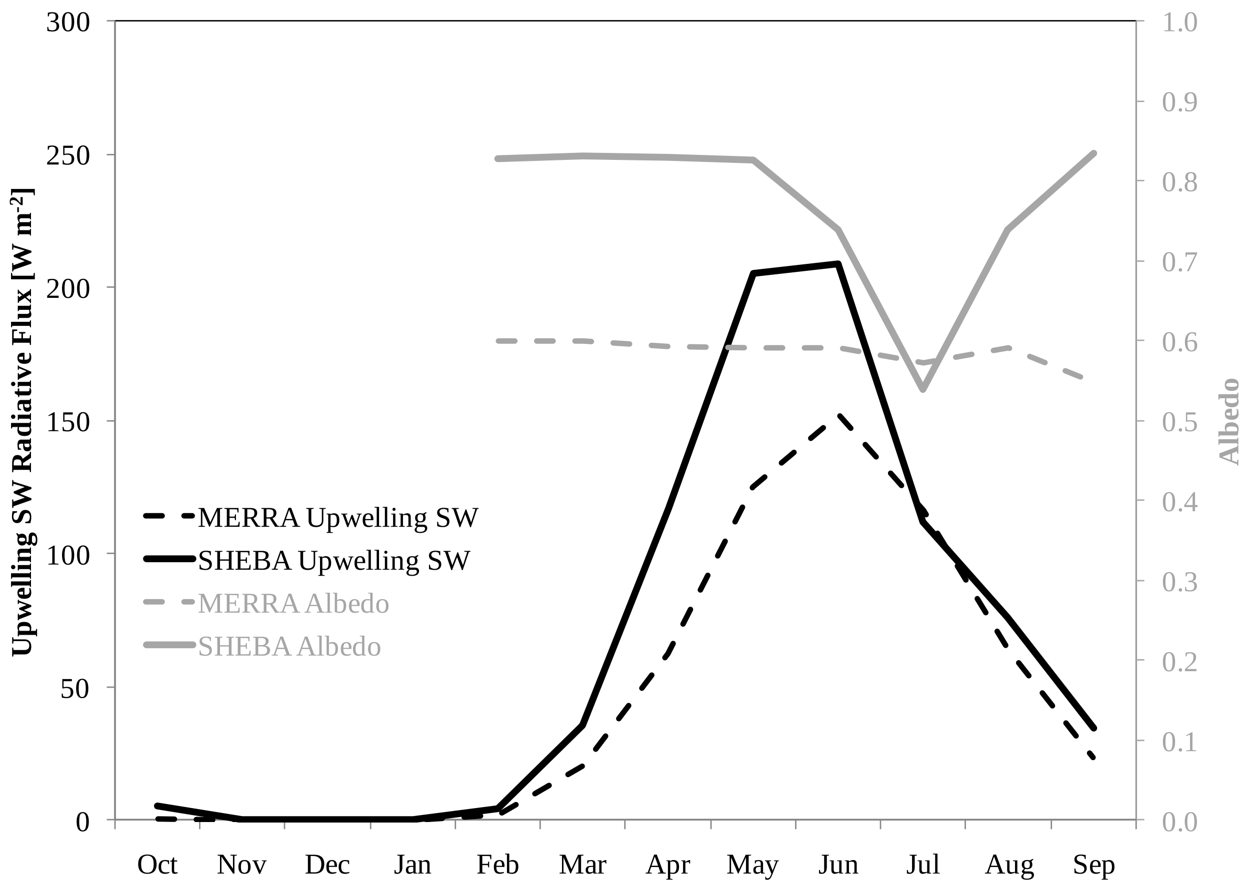

FIGURE 6. Monthly averaged surface albedo (gray) and upwelling shortwave radiative flux (dark) for observed (solid) and corresponding MERRA values (dashed) for October 1997 to September 1998, in W m^{-2}.

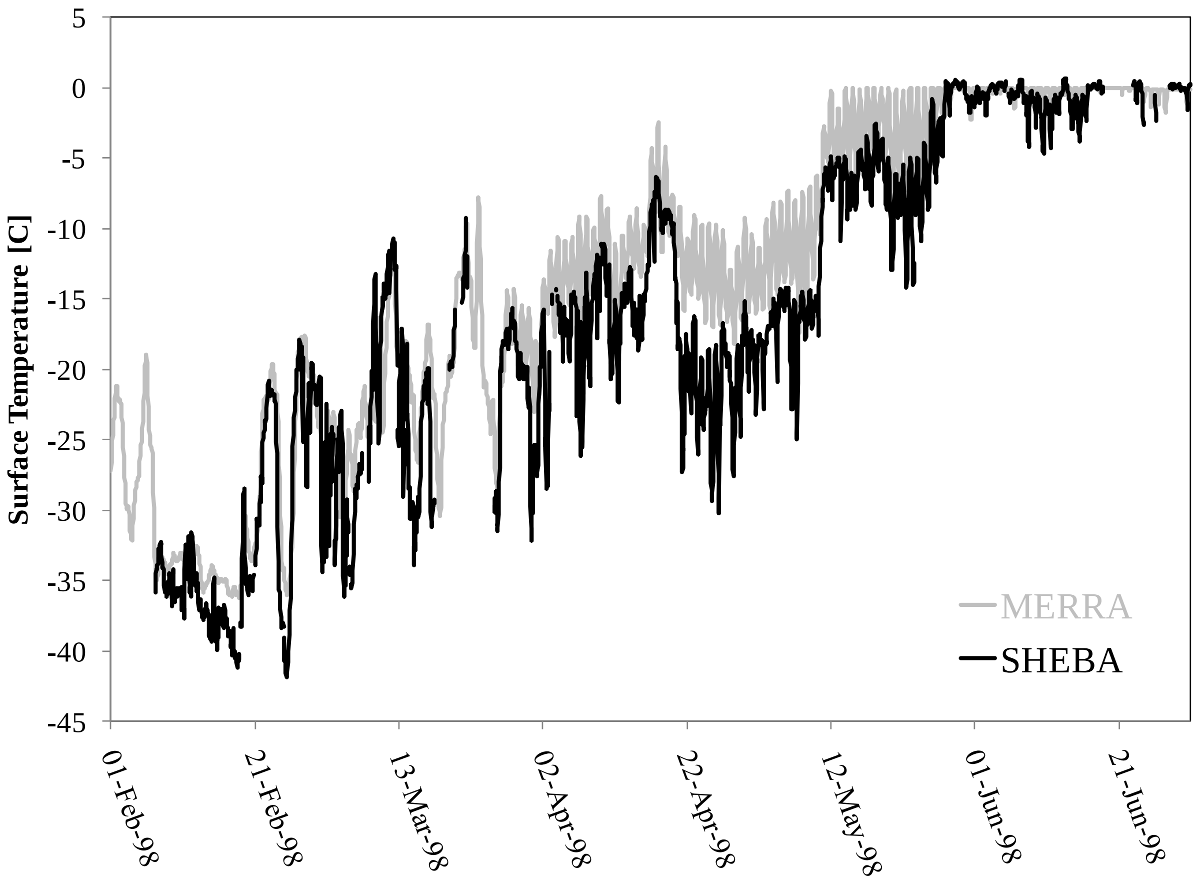

FIGURE 7. Near-surface hourly air temperature from SHEBA and corresponding values from MERRA for the period 1-February 1998 to 30-June 1998, in degrees C.

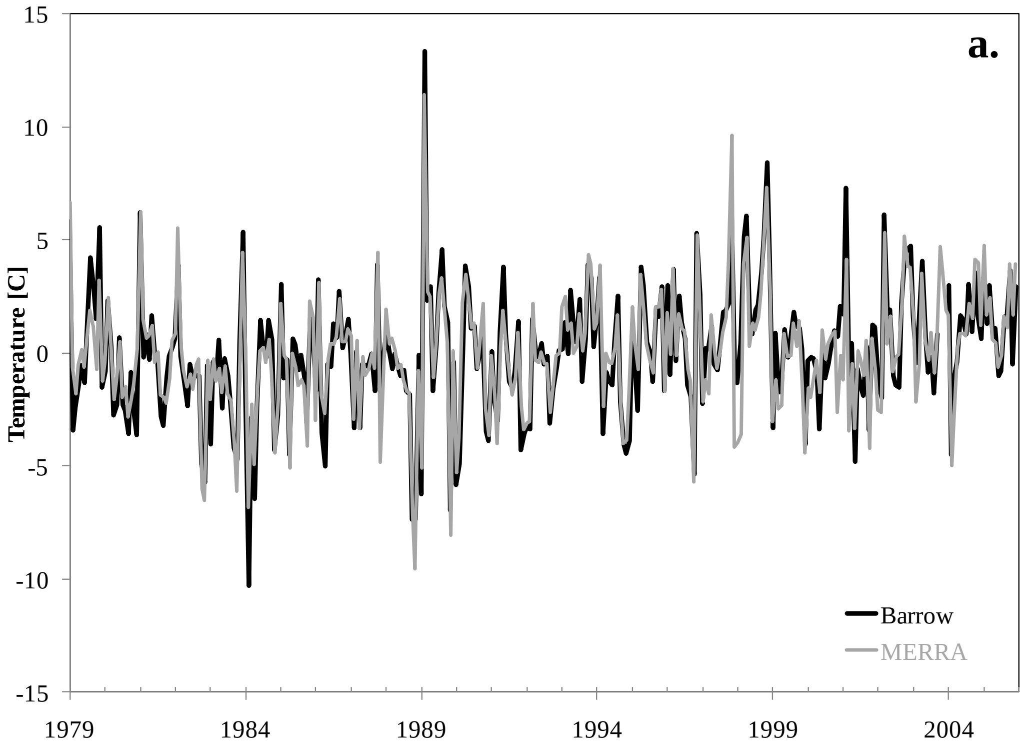

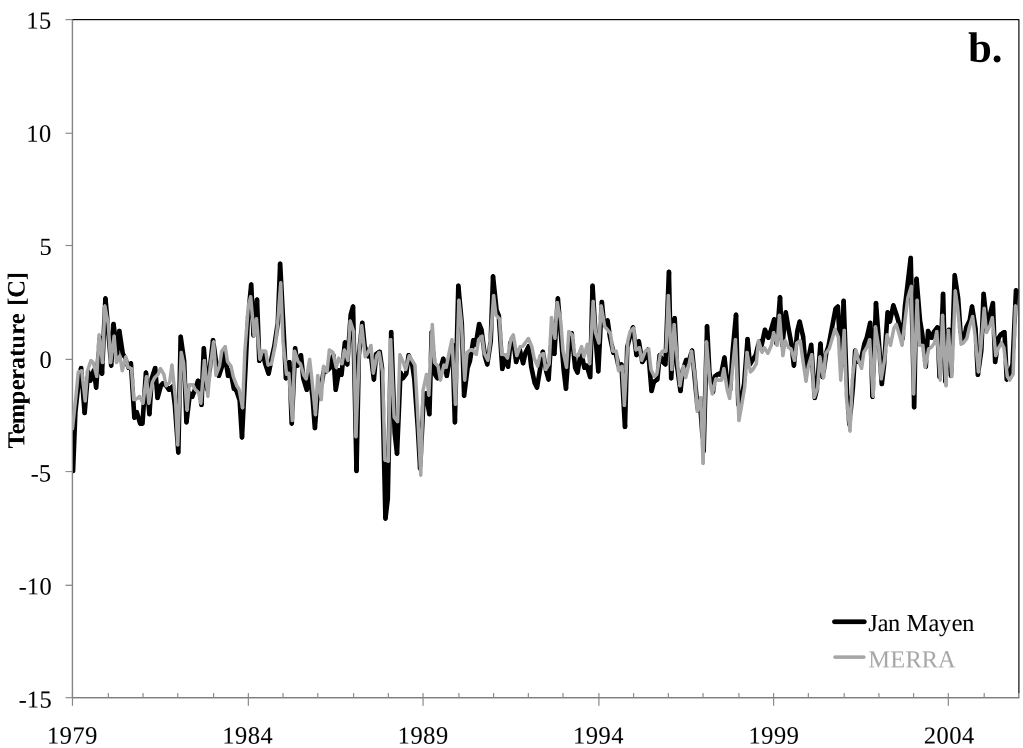

FIGURE 8. Time series of monthly averaged near-surface station air temperature anomaly and corresponding MERRA values for Barrow (left, 71°N, 157°W) and Jan Mayen (right, 71°N, 9°W), in degrees C.

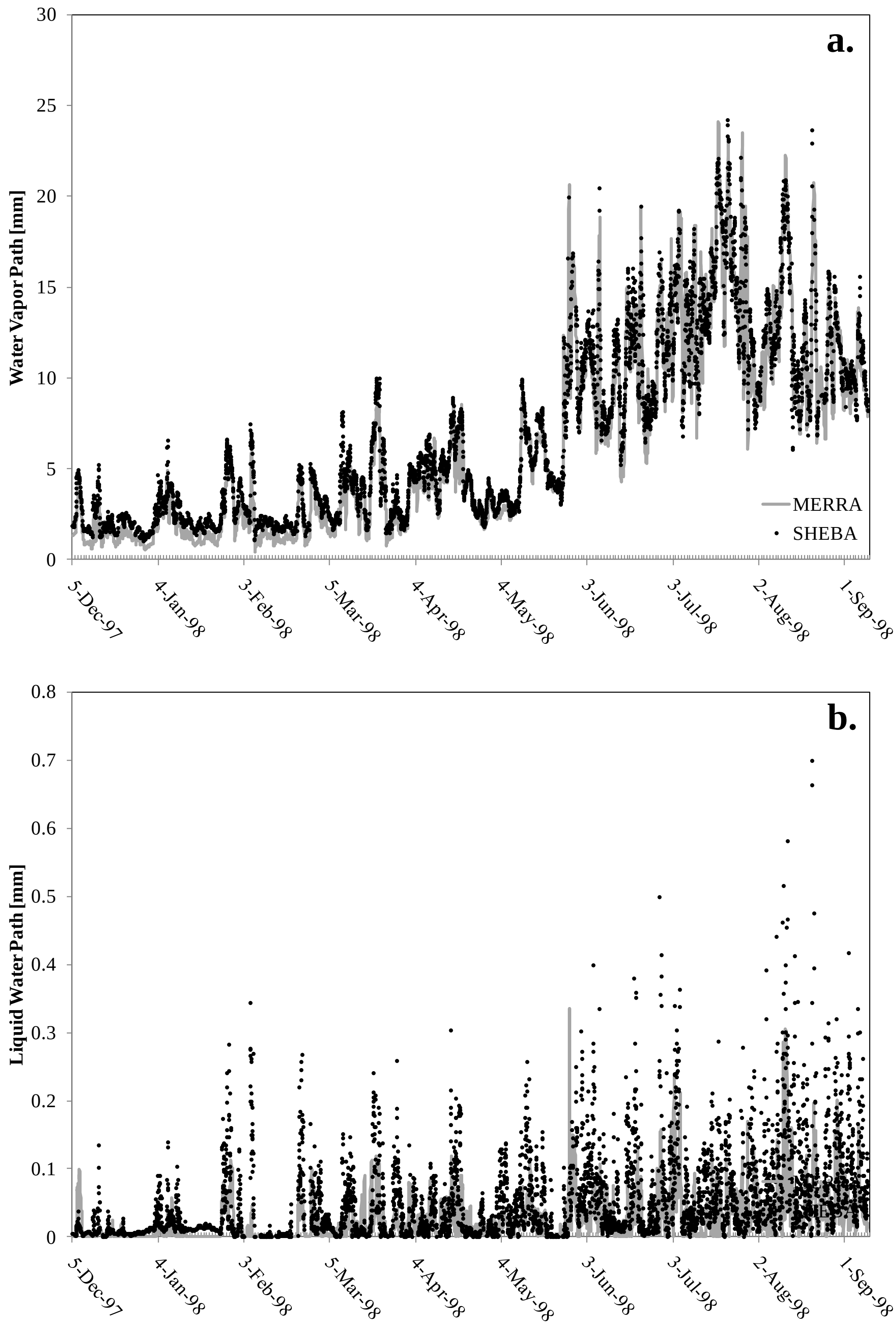

FIGURE 9. Hourly (a.) precipitable water and (b.) liquid water path from SHEBA microwave radiometer and corresponding MERRA values, in mm.

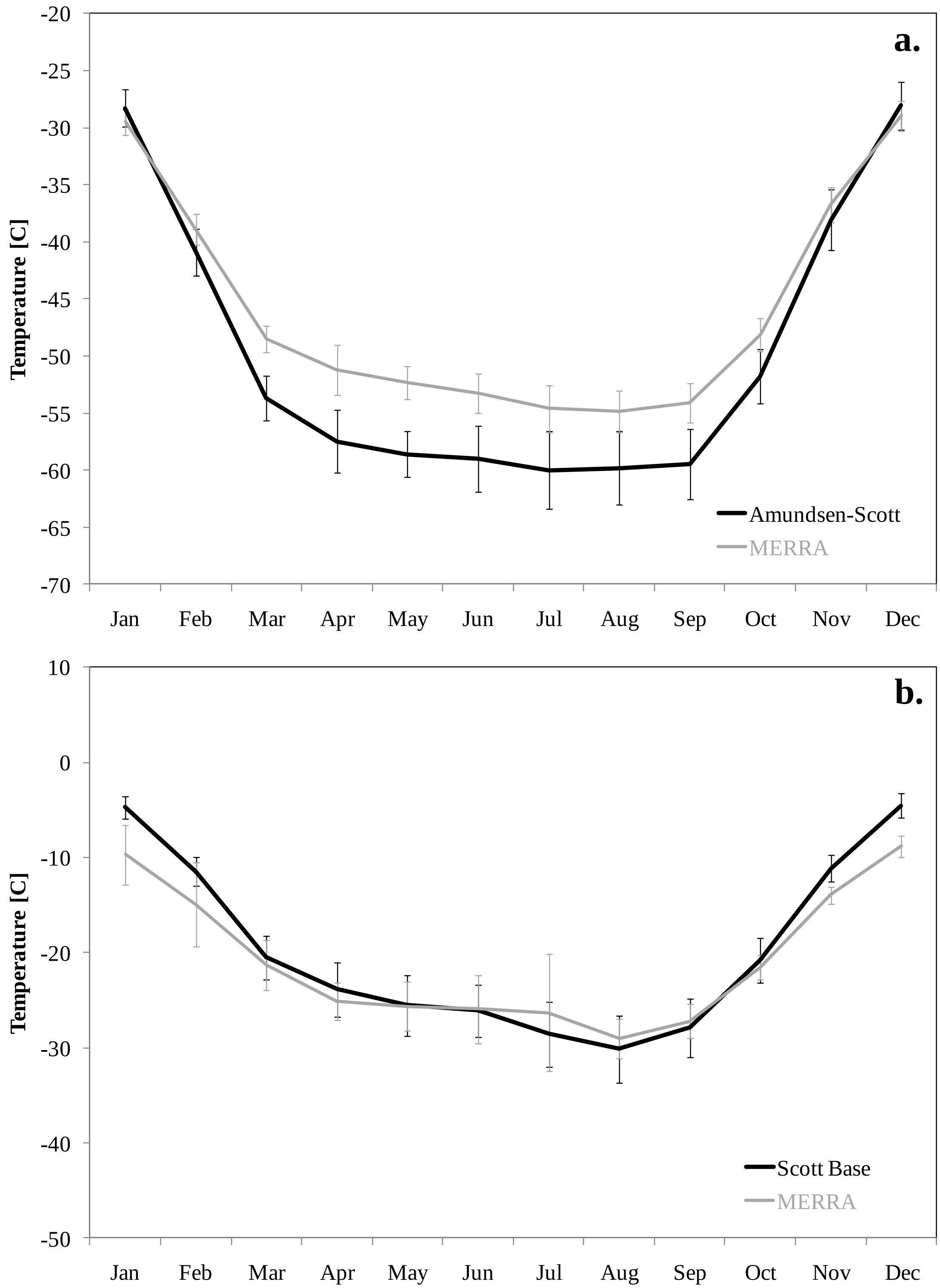

FIGURE 10. Average annual time series for near surface station temperature and corresponding MERRA values for (a.) Amundsen-Scott (90°S), and (b.) Scott Base (78°S, 167°E), in degrees C. Bars indicate the standard deviation of monthly values over the period 1979-2005.

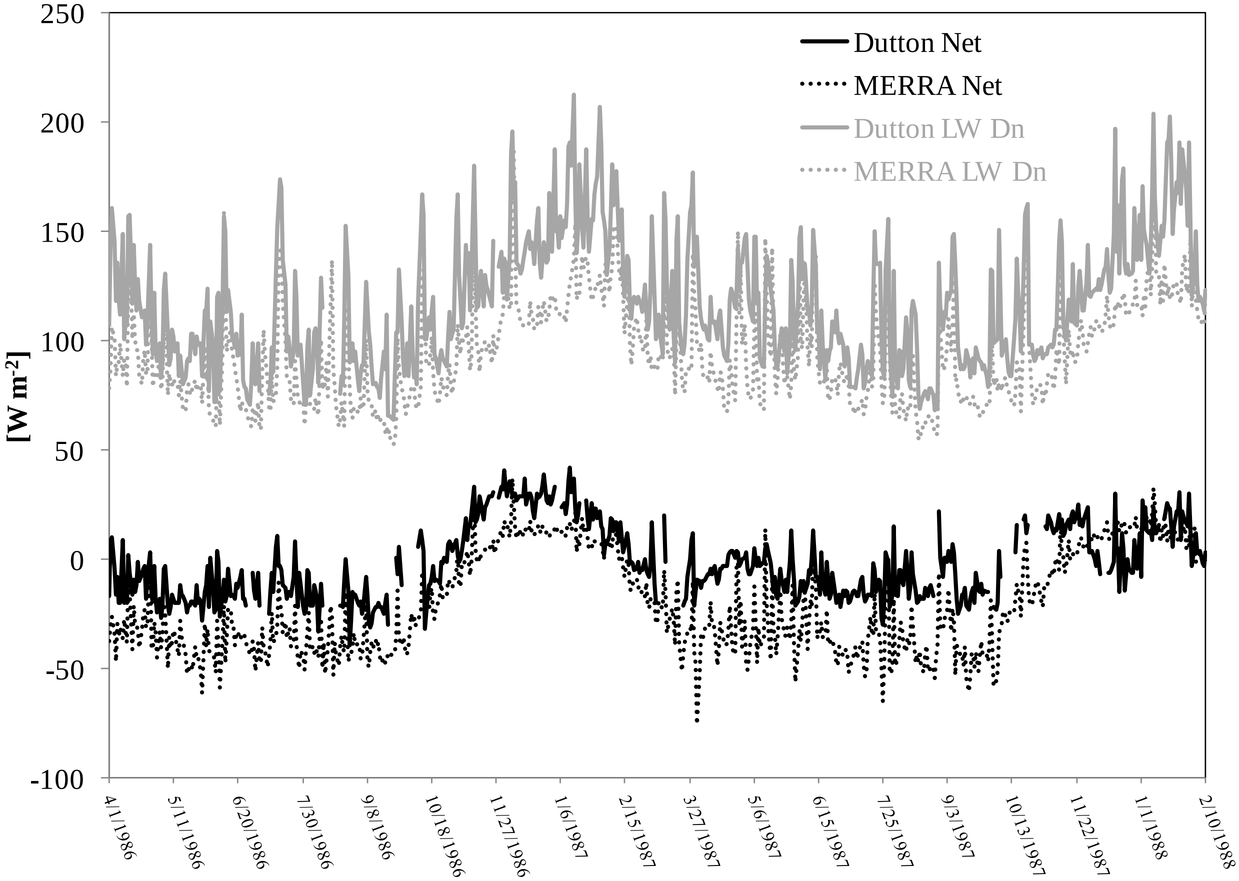

FIGURE 11. Time series of daily downwelling longwave flux and the net downward flux from Dutton et al. (1989) and corresponding values from MERRA for 90°S, in W m^{-2}.